

# Holographic characterization of imperfect colloidal spheres

Mark Hannel, Christine Middleton, and David G. Grier

*Department of Physics and Center for Soft Matter Research, New York University, New York, NY 10003*

We demonstrate precise measurements of the size and refractive index of individual dimpled colloidal spheres using holographic characterization techniques developed for ideal spheres.

Holographic snapshots of colloidal spheres can be interpreted with the Lorenz-Mie theory of light scattering to measure an individual sphere's three-dimensional position, size and refractive index<sup>1</sup>. When applied to dielectric spheres with near-ideal sphericity and smoothness, this technique yields nanometer-scale precision for the position and radius<sup>1-4</sup> and part-per-thousand precision for the refractive index<sup>1,5</sup>. Here, we demonstrate that this technique yields similarly precise and meaningful results for imperfect spheres, provided that their deviation from sphericity is not too pronounced.

Our model system for this work consists of monodisperse colloidal particles synthesized through emulsion polymerization of 3-methacryloxypropyl trimethoxysilane (TPM)<sup>6</sup>. Depending on how they are made, these particles can take the form of spheres, as shown in Fig. 1(a), or dimpled spheres, as shown in Fig. 1(b), in which both the sphere radius and dimple dimensions are drawn from narrow distributions.

The two types of particles are synthesized through similar pathways. TPM oil, which ordinarily is insoluble in water, undergoes hydrolysis in a basic environment (pH > 9) and becomes water soluble. Solubilized monomers then form insoluble oligomers, which condense into spherical droplets. Once the droplets are fully grown, they are solidified through free radical polymerization that is initiated by adding 2,2'-azo-bis-isobutyronitrile (AIBN) and heating to 80 °C for 2 h. The particles then are washed and redispersed in deionized water for study.

Homogeneously nucleated TPM droplets form spheres. To synthesize dimpled spheres, we heterogeneously nucleate droplet condensation by adding 0.65  $\mu\text{m}$ -diameter polystyrene spheres to the aqueous phase. These small spheres serve as nucleation sites for TPM condensation and remain embedded in the surface of the resulting droplet to a depth that depends on their wetting characteristics. They remain in place during polymerization, and thus determine the size of the dimple in the final particle. After the TPM is polymerized, the polystyrene spheres are dissolved by transferring the particles into toluene, leaving uniformly sized dimples. For the sample represented by Fig. 1(b), the dimple accounts for 5 % of the equivalent sphere's volume. The completed particles are then transferred back into deionized water for cleaning and study.

Dimpled spheres have immediate applications for lock-and-key colloidal self-assembly<sup>7-12</sup> and are models for colloidal microcapsules<sup>13</sup>, which are widely used in industrial applications, and tend to buckle into dimpled spheres through osmotic stress<sup>13-15</sup>. They are useful for

assessing the limits of holographic characterization because their departure from sphericity is well defined.

We prepared these particles for holographic characterization by dispersing them in water at a volume fraction of  $10^{-5}$  and introduced into a 50  $\mu\text{m}$ -thick gap between a glass microscope slide and a cover slip. The sample is sealed and mounted on the stage of a custom-built holographic microscope<sup>1,16</sup>, which illuminates it with a collimated laser beam at a vacuum wavelength of  $\lambda = 447 \text{ nm}$  (Coherent Cube). An illuminated particle scatters some of the laser light to the focal plane of a microscope objective lens (Nikon Plan Apo, 100 $\times$ , numerical aperture 1.4, oil immersion) where it interferes with the unscattered portion of the beam. The interference pattern is relayed by the objective lens and a tube lens to a video camera (NEC TI-324A), which records its intensity at 29.97 frames/s with a calibrated magnification of 135 nm/pixel. The camera's 0.1 ms exposure time is short enough to avoid blurring of the interference pattern due to particle motion<sup>17,18</sup>. The illumination is linearly polarized with its axis of polarization aligned to within  $1^\circ$  with the  $\hat{x}$  axis of the camera.

Each video frame is a hologram of the particles in the  $86 \mu\text{m} \times 65 \mu\text{m}$  field of view. The images in Fig. 1(c) and 1(d) are typical holograms of a sphere and a dimpled sphere, respectively. They each subtend  $150 \times 150$  pixel and are cropped from the camera's  $640 \times 480$  pixel field of view. Such holograms then can be analyzed<sup>1,2,17,19</sup> with predictions of the Lorenz-Mie theory of light scattering<sup>20,21</sup> to estimate the particle's radius,  $a_p$  and refractive index,  $n_p$ . Specifically, we process a recorded image  $I(\mathbf{r})$  by subtracting off the camera's dark count,  $I_d(\mathbf{r})$  and normalizing by a background image,  $I_0(\mathbf{r})$ , that is recorded with no particles in the field of view:

$$b(\mathbf{r}) = \frac{I(\mathbf{r}) - I_d(\mathbf{r})}{I_0(\mathbf{r}) - I_d(\mathbf{r})}. \quad (1)$$

Assuming that gradients in the amplitude and phase of the illumination are small over the scale of the particle, the normalized hologram of a particle located at  $\mathbf{r}_p$  relative to the center of the microscope's focal plane may be modeled as<sup>1,4</sup>

$$b(\mathbf{r}) = |\hat{x} + e^{-ikz_p} \mathbf{f}_s(k(\mathbf{r} - \mathbf{r}_p))|^2, \quad (2)$$

where  $k = 2\pi n_m/\lambda$  is the wave number of the light in a medium of refractive index  $n_m$ , and where  $\mathbf{f}_s(k\mathbf{r})$  describes how the particle scatters  $\hat{x}$ -polarized light.

If the particle may be modeled as an ideal isotropic sphere, then  $\mathbf{f}_s(k\mathbf{r})$  is the Lorenz-Mie scattering

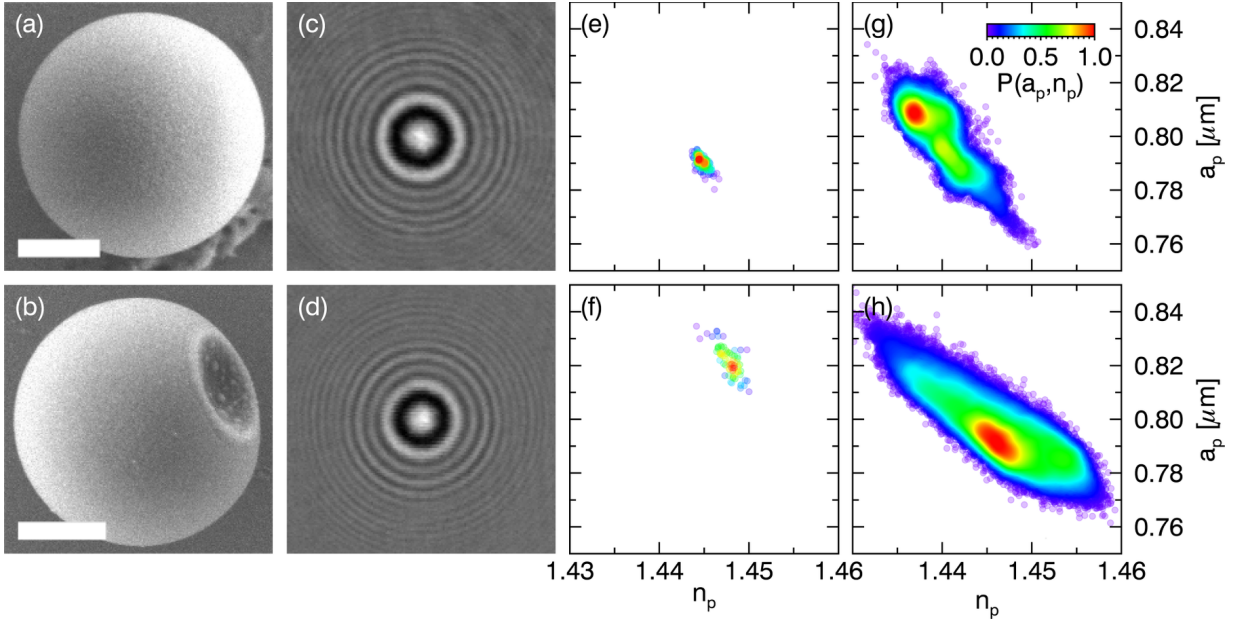


FIG. 1. (a) Scanning electron micrograph of a colloidal TPM sphere and (b) a dimpled sphere. Scale bars represent 500 nm. (c) and (d) Corresponding holograms for particles from the samples show in (a) and (b). (e) 5000 measurements of sphere radius and refractive index for a single TPM sphere held in an optical tweezer. Each point represents a single measurement, and is colored according to the relative density of measurements,  $P(a_p, n_p)$ . (f) equivalent result for a dimpled sphere. (g) Distribution of size and refractive index for 5000 TPM spheres and (h) 5000 dimpled spheres.

function<sup>20,21</sup>, which is parameterized by the particle's radius and refractive index. Fitting Eq. (2) to a measured hologram therefore yields the particle's three-dimensional position  $\mathbf{r}_p$ , its radius  $a_p$  and its refractive index  $n_p$ . Previous studies on model colloidal spheres have confirmed that these fits converge reliably for micrometer-scale spheres, and yield the radius with a precision better than 5 nanometers<sup>1,3,4</sup> and the refractive index to within 3 parts per thousand<sup>3,5</sup>. The data in Fig. 1(e) show results obtained for a typical TPM sphere localized in an optical trap that was projected through the microscope's objective lens using the holographic optical trapping technique<sup>22</sup>. The spread in values is comparable to the numerically estimated uncertainty in the individual fits,  $a_p = 0.790 \pm 0.003 \mu\text{m}$  and  $n_p = 1.445 \pm 0.001$ , suggesting both that the imaging model is appropriate, and also that the signal-to-noise ratio estimated by the median-absolute-deviation (MAD) metric is reasonable. This sphere's holographically measured radius is consistent with the mean value,  $0.76 \pm 0.06 \mu\text{m}$ , obtained through SEM observations on the same batch of spheres. As expected, the polymerized particles' refractive index is larger than that of monomeric TPM oil, 1.431 at the imaging wavelength.

The scattering function for an aspherical object, such as a dimpled sphere, depends on the object's detailed shape and orientation<sup>21</sup>. Analytical results are available for just a few special cases. For more general cases, numerical methods are required, such as the discrete dipole approximation (DDA)<sup>23</sup>. Even with highly optimized

implementations<sup>24</sup>, however, such approaches are computationally intensive<sup>25</sup>. If an object's departure from sphericity is small enough, and if the influence of the non-ideality on the recorded hologram is sufficiently well localized within the recorded image, Lorenz-Mie analysis may still yield useful results for the particle's size and refractive index without incurring this cost.

Figure 1(f) shows results obtained by fitting the ideal-case model to holograms of an optically trapped dimpled sphere. The radius estimated by straightforward Lorenz-Mie analysis of 60 such holograms is  $0.821 \pm 0.006 \mu\text{m}$ . The corresponding estimate for the refractive index,  $1.448 \pm 0.001$  is remarkably similar to the value obtained for the ideal spheres. In both cases, the distribution of values extracted from nonlinear least-squares fits to Eq. (2) is consistent with single-fit error estimates. This agreement suggests that the ideal model can yield quantitative results for the characteristics of dimpled spheres, without incurring the costs of more realistic modeling.

SEM analysis suggests that the sample-averaged radius of the dimpled spheres is  $0.75 \pm 0.05 \mu\text{m}$ , which is significantly smaller than the result obtained holographically. Similar discrepancies have been noted in previous studies<sup>26</sup>, and reasonably may be explained by changes induced by preparing the spheres for SEM observation.

The extent to which a dimpled sphere's hologram may be described with an ideal sphere's scattering function depends on the dimple's orientation. Optically trapping a dimpled sphere constrains its rotations as well as its translations, fixing the dimple's axis in the trans-

verse plane. When released from its trap, the dimpled sphere rotates freely in three dimensions, with consequences for holographic characterization. Figure 1(g) shows the distribution of characteristics obtained over the course of 10 min for a freely diffusing sphere. The mean radius and refractive index obtained for this particle are  $0.80 \pm 0.01 \mu\text{m}$  and  $1.440 \pm 0.003$ , respectively. Additional uncertainty in the particle's radius and refractive index reflects uncorrected interference artifacts in the recorded hologram due to defects in illumination<sup>4</sup>. The corresponding distribution for the freely diffusing dimpled sphere is broadened still further, and displays a strong anticorrelation between radius and refractive index. The peak of this distribution remains at the trapped-particle values,  $a_p = 0.80 \pm 0.01 \mu\text{m}$  and  $n_p = 1.447 \pm 0.005$ , presumably because the randomly oriented particle is more likely to have its dimple transverse to the optical axis than facing it.

Having the dimple pointing sideways is beneficial for holographic characterization. In this orientation, the dimple's contribution to the scattering pattern is asymmetric, and thus minimally influences the fit to the largely symmetric model. It plays a role comparable to uncorrected background artifacts, reducing the precision, but not seriously affecting the mean values. When the dimple is directed along the axis, however, distortions to the scattering pattern are symmetric about the axis and thus affect the fits more strongly.

The success of an idealized model for describing light scattering by a dimpled sphere may be explained at least heuristically by treating the dimple as a volume of the sphere whose scattering is phase-shifted by  $180^\circ$ . The scattering amplitudes for the sphere as a whole and for the dimple scale roughly as their respective volumes. If the dimple's volume is only a small fraction of the sphere's, and if, furthermore, the dimple's contribution is asymmetric, the perturbation should be negligible.

We applied the same technique to characterizing the distribution of properties in monodisperse samples of TPM spheres and TPM dimpled spheres. For these measurements, dispersions of particles at a volume fraction of  $10^{-4}$  were streamed down a channel by a pressure driven flow with a peak speed of  $100 \mu\text{m s}^{-1}$ . This is fast enough to acquire holograms of 5000 spheres in 10 min, but not so fast as to incur artifacts due to motion-induced blurring<sup>17,18</sup>. Results plotted in Fig. 2 for TPM spheres reveal a reasonably symmetric distribution of particle sizes and refractive indexes peaked at  $0.82 \pm 0.02 \mu\text{m}$  and  $1.446 \pm 0.006$ , respectively. These values are consistent both with the single-sphere measurements reported in Fig. 1. The corresponding distributions for dimpled spheres plotted in Fig. 2 become increasingly broad and asymmetric as the relative size of the dimple increases. Particles with 5 % dimple volumes yield a mean refractive index,  $1.444 \pm 0.006$ , consistent with the ideal spheres' value. Increasing the dimple volume to 10 % leads to substantial deviations, with a mean refractive index of  $1.42 \pm 0.03$ . Some variability can be attributed to the

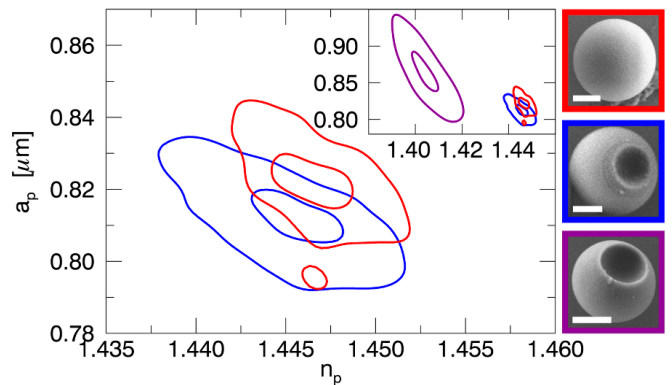


FIG. 2. Level sets of the holographically measured distributions of particle properties for TPM spheres (red), dimpled spheres with small dimples (blue) and large dimples (purple). The presence of a small dimple has no significant influence on holographic characterization results. Larger dimples cause systematic errors. SEM images show typical representatives of each sample, with scale bars denoting 500 nm.

dimpled spheres' random orientation in the channel.

To assess the extent of the distortions that can be handled with the idealized model for holographic characterization, we apply the discrete-dipole approximation<sup>23–25</sup> to compute holograms of dimpled spheres, and then analyze the resulting synthetic data with the same software used to analyze experimental data. The discrete-dipole approximation treats an object as a three-dimensional arrangement of independent microscopic dipole scatterers, each of which is illuminated by the incident beam and also by the first-order scattering of its neighbors<sup>27</sup>. The superposition of scattered waves yields an estimate for  $\mathbf{f}_s(k\mathbf{r})$ , which is used to synthesize a hologram. Dimpled spheres are modeled as the superposition of two spheres separated by a center-to-center distance  $d$ , one of radius  $a_p$  and refractive index  $n_p$ , and the other of radius  $a_d$  and the refractive index of the medium. This is shown schematically in Fig. 3(a). Setting  $a_d = 0$  or  $d \geq a_p + a_d$  yields a perfect sphere. Setting  $d \leq a_p - a_d$  with  $a_p > a_d$  yields a sphere with a spherical inclusion. Dimpled spheres result when  $a_p - a_d \leq d \leq a_p + a_d$ . Lines in Fig. 3(b) demarcate these regions.

Analyzing DDA-generated holograms of perfect spheres yields excellent agreement with input parameters for sphere radii up to  $a_p \leq 0.5 \mu\text{m}$ . Scattering by larger spheres requires proper treatment of higher-order scattering, and is not supported by the ADDA implementation of the DDA algorithm that we adopted<sup>24,25</sup>. Limiting the analysis to parameters within the spherical particle's domain of applicability, we assessed discrepancies between input parameters and values obtained by fitting the resulting holograms with the scattering function for ideal spheres.

Figure 3 summarizes the performance of Lorenz-Mie analysis for characterizing dimpled spheres. Values in Fig. 3(b) represent the factor by which the error in a

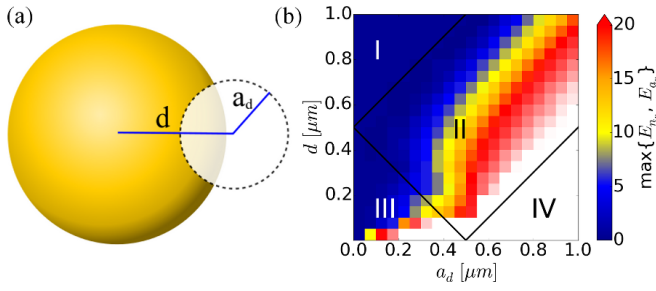


FIG. 3. Holographic characterization of dimpled TPM spheres with radius  $a_p = 0.5 \mu\text{m}$  as a function of dimple radius  $a_d$  and inset distance,  $d$ . (a) Schematic representation of sphere geometry. (b) Relative error as a function of dimple radius and offset. Colors represent the larger of the errors in particle radius and refractive index, relative to their respective estimated uncertainties. Region I represents ideal spheres. Region II: dimpled spheres. Region III: spheres with spherical inclusions. Region IV: inaccessible.

dimpled particle's measured characteristics in increased relative to the error for an ideal sphere. As anticipated, errors in estimates for a particle's radius and refractive index are smaller than 1% for dimples that take up less than 5% of the sphere's volume. Deviations become larger for spheres distorted by larger dimples, particularly if those dimples are aligned with the optical axis. This leaves a substantial domain of applicability within which computationally efficient implementations of hologram analysis can be used to measure the properties of this class of imperfect spheres.

This work was supported primarily by the MRSEC program of the National Science Foundation through Grant Number DMR-1420073, in part by the NSF through Grant Number DMR-1305875, in part by the U.S. Army Research Office under Grant Award No. W911NF-10-1-0518 and in part by a grant from Procter & Gamble. The holographic characterization instrument was developed under support of the MRI program of the NSF through Grant Number DMR-0922680. The scanning electron microscope was purchased with financial support from the MRI program of the NSF under Award DMR-0923251.

<sup>1</sup>S.-H. Lee, Y. Roichman, G.-R. Yi, S.-H. Kim, S.-M. Yang, A. van Blaaderen, P. van Oostrum, and D. G. Grier, *Opt. Express* **15**, 18275 (2007), 0712.1738.

<sup>2</sup>F. C. Cheong, B. J. Krishnatreya, and D. G. Grier, *Opt. Express* **18**, 13563 (2010).

<sup>3</sup>H. Moyses, B. J. Krishnatreya, and D. G. Grier, *Opt. Express* **21**, 5968 (2013).

- <sup>4</sup>B. J. Krishnatreya, A. Colen-Landy, P. Hasebe, B. A. Bell, J. R. Jones, A. Sunda-Meya, and D. G. Grier, *Am. J. Phys.* **82**, 23 (2014).
- <sup>5</sup>H. Shpaisman, B. J. Krishnatreya, and D. G. Grier, *Appl. Phys. Lett.* **101**, 091102 (2012).
- <sup>6</sup>S. Sacanna, M. Korpics, K. Rodriguez, L. Colon-Melendez, S.-H. Kim, D. J. Pine, and G.-R. Yi, *Nature Commun.* **4**, 1688 (2013).
- <sup>7</sup>S. Sacanna, W. T. M. Irvine, P. M. Chaikin, and D. J. Pine, *Nature* **464**, 575 (2010).
- <sup>8</sup>J. Macfarlane, Robert and C. A. Mirkin, *ChemPhysChem* **11**, 3215 (2010).
- <sup>9</sup>S. Sacanna, W. T. M. Irvine, L. Rossi, and D. J. Pine, *Superlattices Microstructures* **7**, 1631 (2011).
- <sup>10</sup>D. J. Ashton, R. L. Jack, and N. B. Wilding, *Superlattices Microstructures* **9**, 9661 (2013).
- <sup>11</sup>C. L. Phillips, E. Jankowski, B. J. Krishnatreya, K. V. Edmond, S. Sacanna, D. G. Grier, D. J. Pine, and S. C. Glotzer, *Soft Matter* **10**, 7395 (2014).
- <sup>12</sup>Y. Wang, Y. Wang, X. Zheng, G.-R. Yi, S. Sacanna, D. J. Pine, and M. Weck, *J. Am. Chem. Soc.* **136**, 6866 (2014).
- <sup>13</sup>T. M. S. Chang, *Science* **146**, 524 (1964).
- <sup>14</sup>S. Knoche and J. Kierfeld, *Phys. Rev. E* **84**, 046608 (2011).
- <sup>15</sup>J. Jose, M. Kamp, A. van Blaaderen, and A. Imhof, *Langmuir* **30**, 2385 (2014).
- <sup>16</sup>S.-H. Lee and D. G. Grier, *Opt. Express* **15**, 1505 (2007).
- <sup>17</sup>F. C. Cheong, B. Sun, R. Dreyfus, J. Amato-Grill, K. Xiao, L. Dixon, and D. G. Grier, *Opt. Express* **17**, 13071 (2009).
- <sup>18</sup>L. Dixon, F. C. Cheong, and D. G. Grier, *Opt. Express* **19**, 4393 (2011).
- <sup>19</sup>B. J. Krishnatreya and D. G. Grier, *Opt. Express* **22**, 12773 (2014).
- <sup>20</sup>C. F. Bohren and D. R. Huffman, *Absorption and Scattering of Light by Small Particles* (Wiley Interscience, New York, 1983).
- <sup>21</sup>M. I. Mishchenko, L. D. Travis, and A. A. Lacis, *Scattering, Absorption and Emission of Light by Small Particles* (Cambridge University Press, Cambridge, 2001).
- <sup>22</sup>E. R. Dufresne and D. G. Grier, *Rev. Sci. Instrum.* **69**, 1974 (1998); D. G. Grier, *Nature* **424**, 810 (2003).
- <sup>23</sup>B. T. Draine and P. J. Flatau, *J. Opt. Soc. Am. A* **11**, 1491 (1994).
- <sup>24</sup>M. A. Yurkin and A. G. Hoekstra, *J. Quant. Spectr. Rad. Trans.* **112**, 2234 (2011).
- <sup>25</sup>J. Fung, R. W. Perry, T. G. Dimiduk, and V. N. Manoharan, *J. Quant. Spectr. Rad. Trans.* **113**, 212 (2012); R. W. Perry, G. N. Meng, T. G. Dimiduk, J. Fung, and V. N. Manoharan, *Faraday Discuss.* **159**, 211 (2012); A. Wang, T. G. Dimiduk, J. Fung, S. Razavi, I. Kretzschmar, K. Chaudhary, and V. N. Manoharan, *J. Quant. Spectr. Rad. Trans.* **146**, 499 (2014).
- <sup>26</sup>Y. Yamada, K. Miyamoto, and A. Koizumi, *Aerosol Sci. Technol.* **4**, 227 (1985); M. Cermola and W.-H. Schreil, *Microscopy Res. Technol.* **5**, 171 (1987).
- <sup>27</sup>The ADDA implementation of the discrete-dipole approximation<sup>24</sup> used for this study discretizes the particle volume on a three-dimensional square grid with an effective lattice constant roughly one-tenth the wavelength of light in the material. Typical numbers of dipoles range from 100 for the smallest particles considered to 18 000 for the largest.